First Measurement of Λ Electroproduction off Nuclei in the Current and Target Fragmentation Regions

T. Chetry,[3] L. El Fassi,[3,*] W. K. Brooks,[5,4,6,7] R. Dupré,[2]
A. El Alaoui,[5] K. Hafidi,[1] K. P. Adhikari,[3] and M. L. Kabir[3]
(The CLAS Collaboration)
[1]*Argonne National Laboratory, Argonne, Illinois 60439*
[2]*Université Paris-Saclay, CNRS/IN2P3, IJCLab, 91405 Orsay, France*
[3]*Mississippi State University, Mississippi State, MS 39762-5167*
[4]*Thomas Jefferson National Accelerator Facility, Newport News, Virginia 23606*
[5]*Universidad Técnica Federico Santa María, Avenida España 1680, Valparaíso, Chile*
[6]*Center for Science and Technology of Valparaíso, Valparaíso, Chile*
[7]*SAPHIR Millennium Science Institute, Santiago, Chile*
(Dated: September 24, 2022)

We report results of Λ hyperon production in semi-inclusive deep-inelastic scattering off deuterium, carbon, iron, and lead targets obtained with the CLAS detector and the CEBAF 5.014 GeV electron beam. These results represent the first measurements of the Λ multiplicity ratio and transverse momentum broadening as a function of the energy fraction (z) in the current and target fragmentation regions. The multiplicity ratio exhibits a strong suppression at high z and an enhancement at low z. The measured transverse momentum broadening is an order of magnitude greater than that seen for light mesons. This indicates that the propagating entity interacts very strongly with the nuclear medium, which suggests that propagation of di-quark configurations in the nuclear medium takes place at least part of the time, even at high z. The trends of these results are qualitatively described by the GiBUU transport model, particularly for the multiplicity ratios. These observations will potentially open a new era of studies of the structure of the nucleon as well as of strange baryons.

The study of the underlying structure of hadrons suggests a dynamical origin of the strong interactions between the confined color objects, quarks and gluons (partons), the building blocks of nuclei. Given that the description of the non-perturbative transition from partonic degrees of freedom to ordinary hadrons cannot be performed within the perturbative Quantum Chromo-Dynamics (QCD) or lattice QCD frameworks, pure phenomenological methods are explored to study low-energy phenomena such as the hadronization process [1, 2]. To this end, deep inelastic electron-nucleon scattering (DIS) has been utilized as a pioneering process on atomic nuclei to access the modified parton distributions, test the hadronization mechanisms, and study color confinement dynamics in the cold nuclear medium [3–5]. In this regime, when the electron emits an energetic virtual-photon (γ^*) that removes the struck quark from the rest of the residual system, it takes a finite time until the reaction products hadronize. These products would, in lepton-nucleus scattering, interact with the surrounding nuclear medium during the formation time, which is approximated at intermediate energies to be of a similar order as nuclear radii [6]. The target nucleus acts then as a femtoscope with unique analyzing power that allows for the extraction of the hadronization time-distance scales. Therefore, the study of scattering off nuclei with different sizes and at various γ^* kinematics probes the space-time evolution of the hadronization mechanism related to the quark propagation and the color field restoration to form regular hadrons [7, 8].

As depicted in Fig. 1, the hadronization process is characterized by two time-scales describing its two phases. After the virtual photon hard scattering, during the production time (τ_p), the struck quark propagates in the medium as a colored object and thus emits gluons (even in vacuum). This quark then transforms into a colorless object, referred to as a prehadron, which eventually evolves into a fully dressed hadron within the formation time (τ_f). The hadronization studies are thus performed to provide information on the dynamics scales of the process, and constrain the existing models that provide different predictions of its time characteristics either in vacuum or in nuclei [9–13]. In principle, the production and formation mechanisms are the same for both cases with the exception that in the former, the $q\bar{q}$ pairs or qqq systems are considered emerging from the vacuum before expanding into color singlet hadrons, while in the latter, the struck quark is propagating and picking its partner(s) from the medium. In this case, the presence of the medium will lead to several modifications and in-medium stimulated effects related either to the struck quark, formed prehadron, and/or hadron interactions with their surroundings.

The study of hadronization mechanisms is done in the framework of semi-inclusive DIS (SIDIS), and its characteristics are probed via the measurement of two experimental observables. The first is the hadron multiplicity ratio, R_h^A, which is defined as

$$R_h^A(\nu, Q^2, z, p_T^2) = \frac{N_h^A(\nu, Q^2, z, p_T^2)/N_e^A(\nu, Q^2)}{N_h^D(\nu, Q^2, z, p_T^2)/N_e^D(\nu, Q^2)}, \quad (1)$$

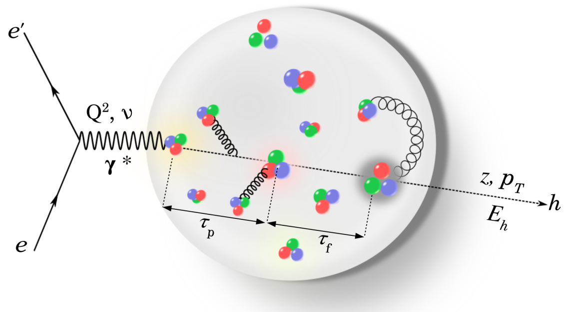

Figure 1. An illustration of the hadronization process as well as its production, τ_p, and formation, τ_f, time-scales. $\nu = E_e - E_{e'}$ is the γ^* energy transferred to the struck quark, Q^2 is the four-momentum transfer squared, $z = E_h/\nu$ is the fractional energy of the observed hadron, h, where E_h is the hadron's energy in the lab frame, and p_T is the hadron's transverse momentum with respect to the virtual-photon direction (see Fig. 2 top-right).

where N_e^A and N_h^A are, respectively, the scattered electron and SIDIS hadron yields produced on a target A and corrected for detector acceptance and reconstruction efficiency. The variables ν, Q^2, z, and p_T are defined in Fig. 1. The multiplicity ratio is normalized by DIS electrons originating from corresponding targets to cancel, to some extent, the initial-state nuclear effects and thus correct for the European Muon Collaboration (EMC) effect [7]. R_h^A quantifies to which extent hadrons are attenuated at a given kinematics as was reported in earlier studies by SLAC [3], HERMES [14–18], and EMC [4] due to the (pre)hadron elastic or inelastic scattering and/or the energy loss of the hadron-fragmented struck quark during the color-neutralization stage preceding hadron formation.

The second observable is the transverse momentum broadening, Δp_T^2, defined as

$$\Delta p_T^2 = \langle p_T^2 \rangle_A - \langle p_T^2 \rangle_D, \qquad (2)$$

where $\langle p_T^2 \rangle_A$ is the mean p_T squared for a target A (see Fig. 2 bottom-right). This observable carries crucial information about the interaction of the propagating parton with the surrounding color field in the nucleus. Several models correlate the p_T-broadening with the parton energy loss triggered by the stimulated gluon bremsstrahlung while crossing the medium in the color-neutralization stage [19, 20]. Based on the perturbative view of the Lund string model, the propagating quark's energy loss is predicted to be at a rate comparable to its string constant on the order of 1 GeV/fm [9, 21]. This effect is believed to be the reason behind the observed jet quenching in heavy-ion collisions at the Relativistic Heavy Ion Collider and at the Large Hadron Collider, leading to the suppression of large p_T hadron production in nucleus-nucleus compared to proton-proton collisions [22, 23].

In this Letter, results on SIDIS production of Λ hyperons off nuclei, *i.e.*, $e+A \to e'+\Lambda+X$, are reported, where A is the heavy nuclear target or deuterium, X is the unobserved hadronic system, and Λ is identified in the final state through its decay products π^- and p. The results represent the first-ever measurement of Λ multiplicity ratios and p_T-broadening as a function of z and the atomic mass-number, A, for the latter in the current (forward) fragmentation region, in which the struck (di-) quark initiates the hadronization process, and the target (backward) fragmentation region, in which the target remnant moves reciprocally with regard to the γ^* direction undergoing a spectator or target fragmentation. Furthermore, the current and target fragmentation processes are assumed to have dominant contributions in distinct phase space regions, which are kinematically separated via the coverage of the Feynman scaling variable x_F [24, 25].

Previous measurements of R_h^A for various hadrons, mainly mesons and (anti-) protons by the HERMES [14–18] and the CLAS [26, 27] Collaborations have reported a strong suppression of leading hadrons at high z and a slight enhancement of multiplicity ratios at low z while scanning heavy to light nuclei. This inverted effect for slow (backward) and fast (forward) protons in HERMES results, the sole baryon study so far, demonstrates the importance of separating the two regions to properly interpret the data. This separation is possible via the z-dependence of the Feynman x_F [28] given that the current fragmentation (high z) is dominated by positive x_F, while the target remnant favors negative x_F [24, 25, 29].

A study of Δp_T^2 for mesons was also performed by the HERMES experiment [17], but its finding was inconclusive due to the similar behavior of its $A^{1/3}$ and $A^{2/3}$ mass-dependencies, for which $A^{1/3}$ is proportional to the nuclear radius and thus the crossed path length, L, in the nuclear medium, while $A^{2/3}$ encodes information about the partonic energy loss as $\Delta E \propto L^2$, which also implies the L-dependence of Δp_T^2 given that $\frac{\Delta E}{dx} \propto \Delta p_T^2$ [19, 20].

The data presented in this paper were collected during early 2004. An electron beam of 5.014 GeV energy was incident simultaneously on a 2-cm-long liquid-deuterium target (LD2) and a 3 mm diameter solid target (carbon, iron, or lead). A remotely controlled dual-target system [30] was used to reduce systematic uncertainties and allow high-precision measurements of various experimental observables [27, 31]. The cryogenic and solid targets were located 4 cm apart to minimize the difference in CLAS acceptance while maintaining the ability to identify event-by-event the target where the interaction occurred via vertex reconstruction [32]. The thickness of each solid target (1.72 mm for C, 0.4 mm for Fe, and 0.14 mm for Pb) was chosen so that all targets including deuterium would have comparable **per-nucleon** luminosities ($\sim 10^{34}$ cm^{-2} s^{-1}). The scattered electrons, negative pions, and protons were detected in coincidence using the CLAS spectrometer [33]. The scattered electrons were identified requiring a coincidence between the **Cherenkov** counter and the electromagnetic calorimeter signals [31], while pions and protons were identified through time-of-flight measurements [31, 32, 34].

The Λ hyperons were identified through the reconstructed invariant mass of detected pions and protons (see SP.1 for more details about Λ identification method). For each event, several kinematic variables were evaluated including Q^2, the virtual photon-nucleon invariant mass squared W^2, and the γ^* energy fraction $y = \nu/E_e$, where E_e is the incident beam energy. The SIDIS Λ events were selected with $Q^2 > 1$ GeV^2 to probe the nucleon structure, $W > 2$ GeV to suppress contamination from the resonance region, and $y < 0.85$ to reduce the size of radiative effects on the extracted multiplicity ratios based on the HERMES studies [14–18]. The (p, π^-) invariant mass distributions are shown in Fig. 2 left for iron (top) and LD2 (bottom) with all cuts applied. The distributions exhibit a clean Λ peak positioned around 1115.7 MeV sitting on a substantial combinatorial background (CB). An advanced data modeling and fitting toolkit `RooFit` [35] was used along with the event mixing technique to subtract the CB (red dotted curves in Fig. 2 left), which is reconstructed by combining uncorrelated p and π^- tracks from different events [36]. The extraction of the background-subtracted Λ yields, as well as the p_T^2 means, was performed after weighting their distributions event-by-event with the inverse of the acceptance correction (AC) efficiency factors. The latter were evaluated using events generated with the Pythia event generator [37] and processed by the CLAS GEANT3 package [38] to simulate the detector geometrical acceptance, as well as the associated detection and reconstruction efficiencies. Pythia was modified to include nuclear parton distribution functions [39] and Fermi motion based on the Paris potential distribution and realistic many-body calculations [40]. Radiative effects were also included in the simulation using the RadGen code [41] developed to correct lepton-nucleon scattering observables from Quantum Electrodynamics radiative processes. Small corrections were also applied for other effects related to proton energy loss, scattering angle and momentum distortions, vertex misalignment [32, 34], and LD2 endcap contamination.

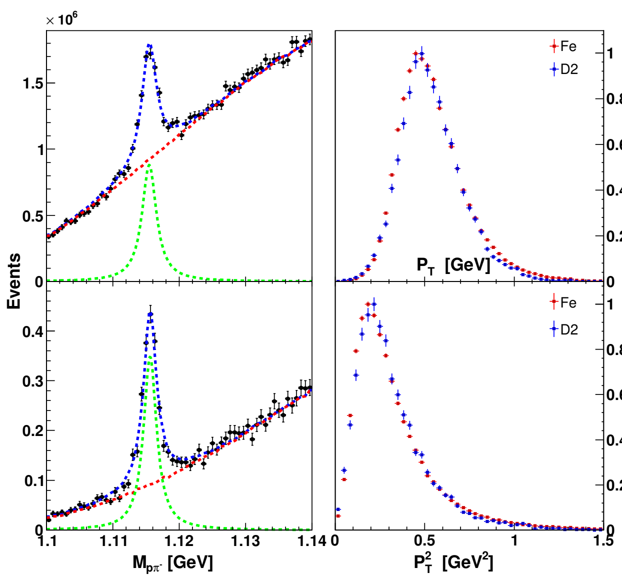

Figure 2. Left: Acceptance-weighted (p, π^-) invariant mass distributions for the Fe/LD2 (top/bottom) targets. Blue curves represent the `RooFit` χ^2 minimization using a simple Breit-Wigner (BW) function for the Λ signal and event mixing for the combinatorial background (red dotted curves). The green distributions are the fit results that are integrated to obtain the Λ yields. Right: Comparison of Fe (red) and LD2 (blue) acceptance-weighted p_T/p_T^2 (top/bottom) normalized distributions to their peak height.

Due to the limited statistics of the Λ production channel, the extractions of both multiplicity ratios and p_T-broadening results were performed by integrating over all kinematic variables except z, which is divided into the six bins shown in Table S6. Given that the interest in this work is in the z and A dependencies of the observables, the systematic uncertainties were separated into point-to-point (p2p), which exhibit some z and A dependencies, and the normalization uncertainties, which are kinematics independent. An in-depth study was carried out and the main systematic sources are related to 1) particle identification cuts to identify the three final-state particles, scattered electron, p, and π^-, 2) dual-target vertex corrections, 3) AC multidimensional (6D) efficiency map variables and the binning that was chosen based on the comparison of experimental data and simulation, 4) AC weight cuts to suppress artificial spikes due to poor statistics in some 6D efficiency bins, 5) CB subtraction methods by varying the event mixing uncorrelated track combinations and BW shapes utilized in `RooFit` for R_Λ^A while considering CB sideband subtraction for Δp_T^2, 6) Λ mass range for R_Λ^A, and 7) LD2 endcaps and radiative correction procedures. As a result, the total p2p (normalization) uncertainties vary between 6% to 30% (less than 3%) for the multiplicity ratios of all nuclei with the dominant contributions from the AC and CB subtraction methods (see Table S3). Similarly, the total p2p uncertainties vary between 10% (1.4%) and 81% (8.5%) for the nuclear z (A) dependence of p_T-broadening (see Table S4 (S5)), while the total normalization uncertainty for both dependencies is less than 1%. The largest p2p z-dependent uncertainty, which is associated with the lead target, is still less than the 50% statistical uncertainty as shown in Fig. 3.

The Λ multiplicity ratio results are depicted in Fig. 3 along with theoretical calculations from the GiBUU model [42]. As expected, R_Λ^A manifests an inverted behavior in the two z-regions; at high z (see Fig. 3 right), the region in which the current fragmentation dominates, Λ baryons exhibit less attenuation in lighter nuclei and

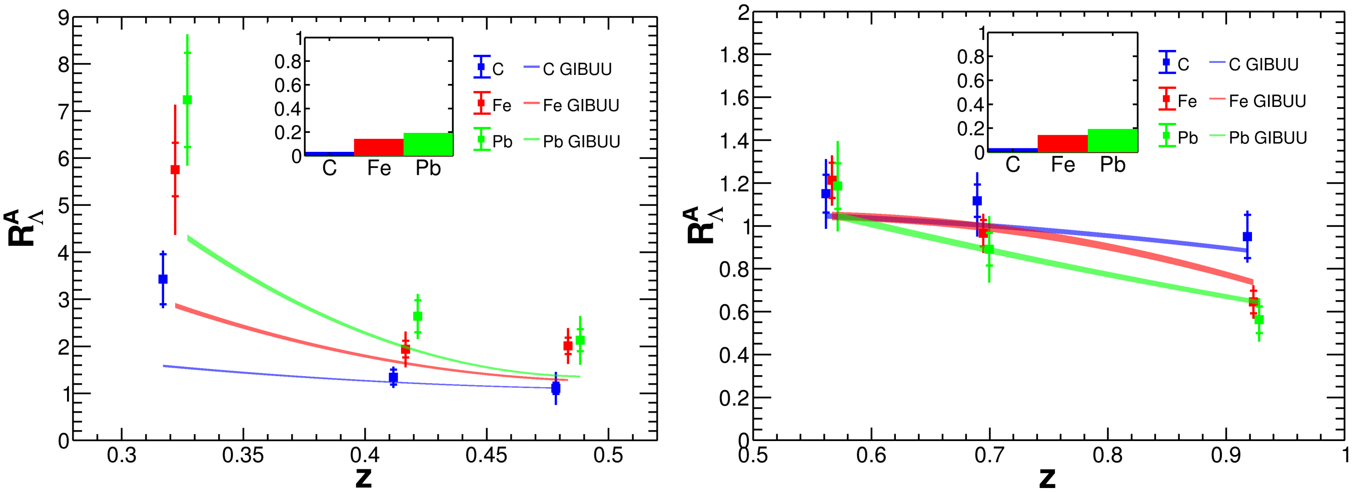

Figure 3. Λ z-binned multiplicity ratios for carbon, iron, and lead (the results are horizontally shifted for clarity). The outer error bars are the p2p systematic uncertainties added in quadrature with the statistical uncertainties. The inset contains the total normalization uncertainties for each nucleus. Left (right) illustrates the results of the low z (high z) region corresponding to the target (current) fragmentation region. The curves correspond to GiBUU model calculations [42].

greater suppression with z, up to 40% in lead and 35% in iron at the highest z-bin. However, at low z (see Fig. 3 left) R^A_Λ is more enhanced on heavy nuclei as a signature of the significant contribution from the target fragmentation that predominates in this kinematic region. This observation is consistent with the fact that the Λ baryons show a significant leading particle effect, *i.e.*, they carry a substantial fraction of the incoming proton momentum [43] and thus large negative x_F (see Fig. S1) and small p_T relative to the γ^* direction [24, 25]. The data are qualitatively described by GiBUU for most of the z-range and most of the targets except for the lowest z-bin, where approximately a factor of two difference is observed.

Figure 4 contains the Λ p_T-broadening results as a function of z (left) and A (right) along with theoretical calculations from the GiBUU model [42]. The monotonic increase of broadening with z and the mass-number reflects the interaction of the propagating object with the surrounding color field in the nucleus during the neutralization stage and/or the elastic scattering of the prehadron and the fully formed Λ [19, 20]. Such a (pre)hadron interaction, as well as broadening, seems to diminish at the highest z-bin. This is an indication of the partonic stage dominance of the hadronization process preceding the (pre)hadron formation, as their elastic scattering in the medium should have led to more broadening as z approaches unity [17, 44]. This trend is in-favor of the $A^{1/3}$ dependence of Δp_T^2 and implies that the production time is within the nuclear medium. Yet, the measured Λ hyperon broadening is an order of magnitude greater than that seen in the HERMES meson results [17]. This could be due to the quark-diquark nucleon structure so that the virtual photon, instead of being absorbed by a quark, is absorbed by a di-quark. That is to say, the propagating colored di-quark has a sizeable mass and an extended QCD color field compared to a single quark, leading to more in-medium interactions, and thus an increase of the Δp_T^2 magnitude [45]. This di-quark scattering speculation offers a good explanation of the R^A_Λ attenuation with increasing z in the current fragmentation region. While GiBUU has reasonably described HERMES, EMC [6, 46, 47], and CLAS [26, 27] multiplicity ratio measurements, it underestimates our Λ p_T-broadening results, which could indicate that the angular distribution is inaccurate in the initial elementary production process of Λ or that the final state interactions in the current model's string fragmentation functions are not realistic [48].

In summary, the first-ever measurement of Λ multiplicity ratios and p_T-broadening as a function of z and A in the current and target fragmentation regions are reported. Both observables depend strongly on z, with an enhancement of R^A_Λ at low z and a suppression at high z up to 0.951 ± 0.125 for carbon, 0.645 ± 0.164 for iron, and 0.562 ± 0.219 for lead, and an increase of p_T-broadening with A and z except for the last z-bin where the broadening starts decreasing due to the partonic stage dominance of the hadronization process. The one order of magnitude larger broadening for this hyperon channel compared to HERMES meson results, as well as the strong suppression of R^A_Λ at high z, suggests the possibility of a direct scattering off di-quark configurations of the nucleon. The multiplicity ratio results are qualitatively described by the GiBUU transport model, however, the model strongly underestimates our p_T-broadening results. This finding has the potential to stimulate further experimental and theoretical inves-

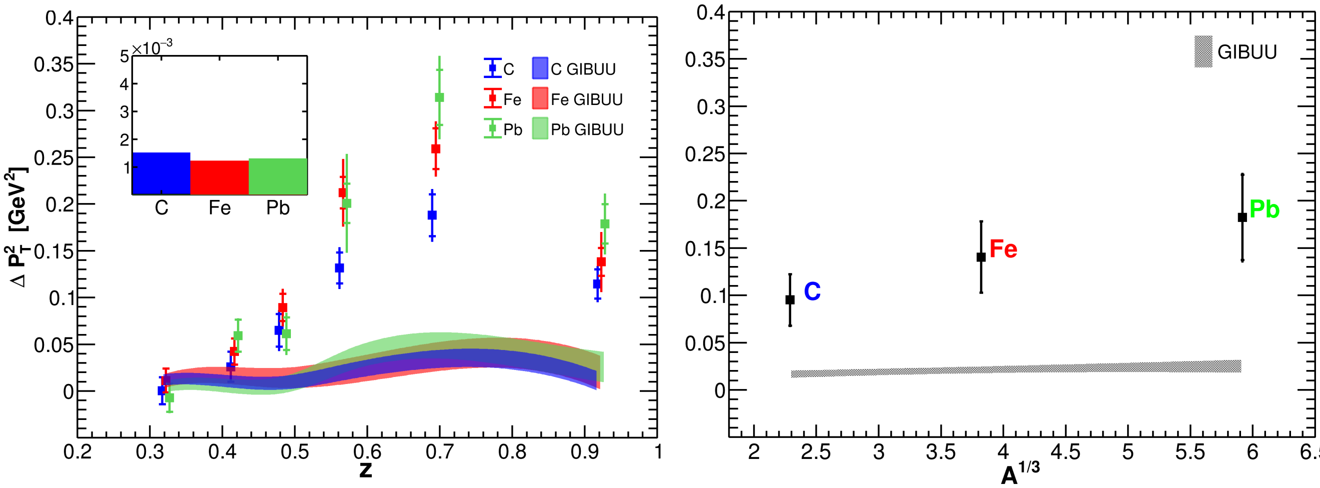

Figure 4. Left (right): The z (nuclear radius)-dependent Δp_T^2 results for the three nuclei (results are horizontally shifted for clarity). The outer error bars are the p2p systematic uncertainties added in quadrature with the statistical uncertainties, while the normalization uncertainties are presented in the inset for the z-dependence and found to be less than 1% for the A-dependence. The GiBUU model calculations are represented by the colored (left) and shaded (right) bands obtained by interpolating the model points and their statistical uncertainties.

tigations, constrain existing models such as GiBUU, and open a new era of studies of the nucleon and light hyperon structure.

Future higher-luminosity measurements with CLAS12 and an 11 GeV beam energy [49] will study SIDIS production of a variety of mesons and baryons over a wide kinematic range. This is crucial to constrain competing models and boost our understanding of the fragmentation mechanisms that lead to the formation of various hadrons. It would also provide an opportunity to study for the Λ SIDIS final states the correlation between kaons and Λs that will presumably be sensitive to the di-quark structure in the struck nucleon. The forthcoming experiments with CLAS12, in addition to measurements at the planned Electron Ion Collider [50], have the potential to investigate in great detail the speculated di-quark scattering in the current results, which would have a significant impact on our understanding of nucleon and baryon structure.

ACKNOWLEDGMENTS

The authors would like to thank K. Gallmeister and U. Mosel for the fruitful discussions on the GiBUU model predictions for this Λ production channel. We acknowledge the staff of the Accelerator and Physics Divisions at the Thomas Jefferson National Accelerator Facility who made this experiment possible. This work was supported in part by the U.S. Department of Energy, the Physics and Astronomy Department and the Office of Research and Economic Development at Mississippi State University, the Chilean Agencia Nacional de Investigacion y Desarrollo (ANID), including by ANID PIA/APOYO AFB180002, ANID PIA ACT1413, and ANID – Millennium Program – ICN2019_044, by the Italian Istituto Nazionale di Fisica Nucleare, the French Centre National de la Recherche Scientifique, the French Commissariat á l'Energie Atomique, the United Kingdom Science and Technology Facilities Council (STFC), the Scottish Universities Physics Alliance (SUPA), the National Research Foundation of Korea, and the U.S. National Science Foundation. The Southeastern Universities Research Association operates the Thomas Jefferson National Accelerator Facility for the United States Department of Energy under Contract No. DE-AC05-06OR23177.

* le334@msstate.edu

[1] D. J. Gross and F. Wilczek, Ultraviolet behavior of non-abelian gauge theories, Phys. Rev. Lett. **30**, 1343 (1973).

[2] Y. L. Dokshitzer, QCD phenomenology (2003) pp. 1–33, arXiv:hep-ph/0306287.

[3] L. S. Osborne, C. Bolon, R. L. Lanza, D. Luckey, D. G. Roth, J. F. Martin, G. J. Feldman, M. E. B. Franklin, G. Hanson, and M. L. Perl, Electroproduction of Hadrons From Nuclei, Phys. Rev. Lett. **40**, 1624 (1978).

[4] J. Ashman *et al.* (European Muon Collaboration), Comparison of forward hadrons produced in muon interactions on nuclear targets and deuterium, Z. Phys. C **52**, 1 (1991).

[5] A. Arvidson *et al.* (European Muon Collaboration), Hadron production in 200-GeV μ - copper and μ - carbon deep inelastic interactions, Nucl. Phys. B **246**, 381 (1984).

[6] K. Gallmeister and U. Mosel, Time Dependent Hadronization via HERMES and EMC Data Consis-

tency, Nucl. Phys. A **801**, 68 (2008).
[7] A. Accardi, F. Arleo, W. K. Brooks, D. D'Enterria, and V. Muccifora, Parton Propagation and Fragmentation in QCD Matter, Riv. Nuovo Cim. **32**, 439 (2009).
[8] W. K. Brooks and J. A. López, Estimating the color lifetime of energetic quarks, Phys. Lett. B **816**, 136171 (2021).
[9] B. Andersson, G. Gustafson, and C. Peterson, QUARK JET FRAGMENTATION, Phys. Scripta **19**, 184 (1979).
[10] X. Artru and G. Mennessier, String model and multiproduction, Nucl. Phys. B **70**, 93 (1974).
[11] E. V. Shuryak, Quark-Gluon Plasma and Hadronic Production of Leptons, Photons and Psions, Phys. Lett. B **78**, 150 (1978).
[12] X.-N. Wang, Why the observed jet quenching at RHIC is due to parton energy loss, Phys. Lett. B **579**, 299 (2004).
[13] B. Z. Kopeliovich, J. Nemchik, E. Predazzi, and A. Hayashigaki, Nuclear hadronization: Within or without?, Nucl. Phys. A **740**, 211 (2004).
[14] A. Airapetian *et al.* (HERMES Collaboration), Hadron formation in deep inelastic positron scattering in a nuclear environment, Eur. Phys. J. C **20**, 479 (2001).
[15] A. Airapetian *et al.* (HERMES Collaboration), Quark fragmentation to $\pi^{\pm}$, π^0, $K^{\pm}$, p and $\bar{p}$ in the nuclear environment, Phys. Lett. B **577**, 37 (2003).
[16] A. Airapetian *et al.* (HERMES Collaboration), Hadronization in semi-inclusive deep-inelastic scattering on nuclei, Nucl. Phys. B **780**, 1 (2007).
[17] A. Airapetian *et al.* (HERMES Collaboration), Transverse momentum broadening of hadrons produced in semi-inclusive deep-inelastic scattering on nuclei, Phys. Lett. B **684**, 114 (2010).
[18] A. Airapetian *et al.* (HERMES Collaboration), Multidimensional Study of Hadronization in Nuclei, Eur. Phys. J. A **47**, 113 (2011).
[19] R. Baier, Y. L. Dokshitzer, A. H. Mueller, S. Peigne, and D. Schiff, Radiative energy loss and p(T) broadening of high-energy partons in nuclei, Nucl. Phys. B **484**, 265 (1997).
[20] S. J. Brodsky and P. Hoyer, A Bound on the energy loss of partons in nuclei, Phys. Lett. B **298**, 165 (1993).
[21] B. Andersson, G. Gustafson, G. Ingelman, and T. Sjostrand, Parton Fragmentation and String Dynamics, Phys. Rept. **97**, 31 (1983).
[22] J. Adams *et al.* (STAR Collaboration), Incident energy dependence of pt correlations at RHIC, Phys. Rev. C **72**, 044902 (2005).
[23] K. Adcox *et al.* (PHENIX Collaboration), Formation of dense partonic matter in relativistic nucleus-nucleus collisions at RHIC: Experimental evaluation by the PHENIX collaboration, Nucl. Phys. A **757**, 184 (2005).
[24] F. A. Ceccopieri and D. Mancusi, QCD analysis of Lambda hyperon production in DIS target-fragmentation region, Eur. Phys. J. C **73**, 2435 (2013).
[25] F. A. Ceccopieri, Lambda production in the DIS target fragmentation region, Eur. Phys. J. C **76**, 69 (2016).
[26] A. Daniel *et al.* (CLAS Collaboration), Measurement of the nuclear multiplicity ratio for K_s^0 hadronization at CLAS, Phys. Lett. B **706**, 26 (2011).
[27] S. Morán *et al.* (CLAS Collaboration), Measurement of charged-pion production in deep-inelastic scattering off nuclei with the clas detector, Phys. Rev. C **105**, 015201 (2022).
[28] The frame-dependent Feynman variable $x_F = p_L^*/p_{L^{max}}^*$ is defined as the fraction of the center-of-mass longitudinal momentum carried by the hadron with respect to the γ^* direction in the lab frame.
[29] D. Graudenz, One particle inclusive processes in deeply inelastic lepton - nucleon scattering, Nucl. Phys. B **432**, 351 (1994).
[30] H. Hakobyan *et al.*, A double-target system for precision measurements of nuclear medium effects, Nucl. Instrum. Meth. A **592**, 218 (2008).
[31] L. El Fassi *et al.* (CLAS Collaboration), Evidence for the onset of color transparency in ρ^0 electroproduction off nuclei, Phys. Lett. B **712**, 326 (2012).
[32] B. Schmookler *et al.* (CLAS Collaboration), Modified structure of protons and neutrons in correlated pairs, Nature **566**, 354 (2019).
[33] B. A. Mecking *et al.*, The CEBAF large acceptance spectrometer (CLAS), Nucl. Instrum. Meth. **503**, 513 (2003).
[34] O. Hen *et al.* (CLAS Collaboration), Measurement of transparency ratios for protons from short-range correlated pairs, Phys. Lett. B **722**, 63 (2013).
[35] W. Verkerke and D. Kirkby, The roofit toolkit for data modeling (2003).
[36] T. Mineeva, *Hadronization Studies via π^0 Electroproduction off D, C, Fe, and Pb* (2013).
[37] K. Gallmeister and T. Falter, Space-time picture of fragmentation in PYTHIA/JETSET for HERMES and RHIC, Phys. Lett. B **630**, 40 (2005).
[38] E. Wolin, *GSIM User's Guide Version 1.1* (1996).
[39] A. Buckley, J. Ferrando, S. Lloyd, K. Nordström, B. Page, M. Rüfenacht, M. Schönherr, and G. Watt, LHAPDF6: parton density access in the LHC precision era, Eur. Phys. J. C **75**, 132 (2015).
[40] C. Ciofi degli Atti and S. Simula, Realistic model of the nucleon spectral function in few and many nucleon systems, Phys. Rev. C **53**, 1689 (1996).
[41] I. Akushevich, H. Bottcher, and D. Ryckbosch, RADGEN 1.0: Monte Carlo generator for radiative events in DIS on polarized and unpolarized targets, in *Workshop on Monte Carlo Generators for HERA Physics (Plenary Starting Meeting)* (1998) pp. 554–565, arXiv:hep-ph/9906408.
[42] O. Buss, T. Gaitanos, K. Gallmeister, H. van Hees, M. Kaskulov, O. Lalakulich, A. B. Larionov, T. Leitner, J. Weil, and U. Mosel, Transport-theoretical Description of Nuclear Reactions, Phys. Rept. **512**, 1 (2012).
[43] By convention of the $\gamma^* p$ frame, a negative longitudinal momentum fraction x_F corresponds to final state hadrons moving parallel to the incoming proton direction, thus covering the low z region. However, the positive x_F favors high z, where forward fragmentation governs.
[44] P. Di Nezza, Nuclear attenuation and p(t) broadening in DIS at HERMES, J. Phys. Conf. Ser. **110**, 032009 (2008).
[45] M. Barabanov, M. Bedolla, W. Brooks, G. Cates, C. Chen, Y. Chen, E. Cisbani, M. Ding, G. Eichmann, R. Ent, J. Ferretti, R. Gothe, T. Horn, S. Liuti, C. Mezrag, A. Pilloni, A. Puckett, C. Roberts, P. Rossi, and B. Wojtsekhowski, Diquark correlations in hadron physics: Origin, impact and evidence, Progress in Particle and Nuclear Physics **116**, 103835 (2021).
[46] T. Falter, W. Cassing, K. Gallmeister, and U. Mosel, Hadron formation and attenuation in deep inelastic lepton scattering off nuclei, Phys. Lett. B **594**, 61 (2004).

[47] T. Falter, W. Cassing, K. Gallmeister, and U. Mosel, Hadron attenuation in deep inelastic lepton-nucleus scattering, Phys. Rev. C **70**, 054609 (2004).
[48] K. Gallmeister and U. Mosel, private communication (2022).
[49] W. K. Brooks *et al.* (CLAS Collaboration), Quark propagation and hadron formation, E12-06-117 Experiment (2010).
[50] A. Accardi *et al.*, Electron-Ion Collider: The Next QCD Frontier, Eur. Phys. J. A **52**, 268 (2016).

SUPPLEMENTARY MATERIAL

This appendix contains supplementary information about the Λ identification method in SP.1, the acceptance correction details related to the multidimensional (6D) map variables and binning, weight definition and cut, and its application procedure in SP.2, a summary of the contributions of systematic effects to the total point-to-point uncertainty budget in SP.3, and the reported results in the last two figures of this manuscript as well as a supporting figure, Fig. S1, in SP.4. In Table S6, the z-binned multiplicity ratios are given for all nuclei, while Table S7 (Table S8) contains the transverse momentum broadening as a function of z (A) for all nuclei.

SP.1 Lambda Identification In the sample of reconstructed SIDIS events originating from either the liquid or solid target, one scattered e^- and at least one π^- and p, the decay products of the Λ, were required. To reconstruct the z-binned (π^-, p) invariant mass spectrum for each target, the 4-vector energy-momentum ($P^\mu = (E, p_x, p_y, p_z)$) of all identified negatively charged pions and protons were combined event-by-event as

$$P_\Lambda = P_p + P_{\pi^-}, \tag{S1}$$

where P_Λ, P_p, and P_{π^-} are the 4-vector energy-momentum of the Λ candidates, protons, and π^-s, respectively. Figure 2 left shows the acceptance-weighted invariant mass from solid (top) and liquid (bottom) targets in which the Λ peak sits on a huge combinatorial background (red dotted curves) that is subtracted using `RooFit` to extract the pure Λ yields and thus obtain the presented multiplicity ratios in Fig. 3.

SP.2 Acceptance Correction The adopted acceptance correction for this analysis is based on a bin-by-bin correction method. Its main advantage is that it should be, in principle, independent of the model used in the Monte-Carlo (MC) event generator if the chosen bins are infinitely small. This is very important for this channel since it is not expected that the employed model in Pythia would be realistic enough to perfectly reproduce the data. Based on a comparison between MC and experimental data, the chosen AC six dimensional (6D) map variables and binning are summarized in Tables S1- S2.

Variables	Range	Number of bins	Bin width
W [GeV]	2.00 - 2.80	2	0.4
ν	2.25 - 4.25	3	$0.\overline{6}$
ϕ_{π^-} [deg]	0.0 - 360.0	2	180
$\phi_{e\Lambda}$ [deg]	0.0 - 360.0	3	120
P_Λ [GeV]	0.10 - 4.25	3	$1.38\overline{3}$
z	0.28 - 1.00	6	see Table S2
Total		648	

Table S1. Binning for the AC map, where ν, W, and z were already defined, ϕ_{π^-} is the π^- azimuthal decay angle in the Λ rest frame, $\phi_{e\Lambda}$ is the angle between the leptonic and hadronic planes, and p_Λ is the Λ momentum. Table S2 shows the z bins used as reported in Table S6.

The acceptance efficiency factors are defined for each 6D bin k= (W, ν, p_Λ, ϕ_{π^-}, $\phi_{e\Lambda}$, z) as

$$eff_k = \frac{N_{acc}(W, \nu, p_\Lambda, \phi_{\pi^-}, \phi_{e\Lambda}, z)}{N_{gen}(W, \nu, p_\Lambda, \phi_{\pi^-}, \phi_{e\Lambda}, z)}, \tag{S2}$$

where $N_{gen}(W, \nu, p_\Lambda, \phi_{\pi^-}, \phi_{e\Lambda}, z)$ and $N_{acc}(W, \nu, p_\Lambda, \phi_{\pi^-}, \phi_{e\Lambda}, z)$ are, respectively, the number of generated and accepted events in each bin k. Once these efficiency coefficients were computed, the data were corrected event-by-event

$z-$bin #	1	2	3	4	5	6
z_{min}	0.28	0.38	0.44	0.51	0.60	0.75
z_{max}	0.38	0.44	0.51	0.60	0.75	1.00

Table S2. The z bins used in this analysis.

by a weight $\omega_k = 1/eff_k$, which depends on the bin k to which it belongs. It should be noted that if some 6D AC bins have very small efficiencies due to their poor statistics, an artificially large weight would be attributed to those bins that would lead to spikes in the weighted distributions. To avoid this problem, the following weight cut was adopted to minimize this effect on the weighted distributions:

$$60 < \omega_k \leq 2400. \tag{S3}$$

Furthermore, the effect of this weight cut was estimated and applied as a global correction factor, f_ω, to the extracted results. This estimation was done by weighting the MC accepted N_{acc} events and comparing their sum, $\sum \omega N_{acc}$, to the generated ones as

$$f_\omega = \frac{\sum \omega N_{acc}}{N_{gen}.} \tag{S4}$$

This N_{acc} weighted sum is typically equal to the generated events without the weight cut, however, it is slightly less once applied, leading to various f_ω corrections for each z-binned multiplicity ratio result as the p_T-broadening means are insensitive to this correction.

SP.3 Systematic Uncertainties Budget This section contains the contribution of various systematic effects to the reported total point-to-point systematic uncertainty budget for the Λ multiplicity ratios of all nuclei in Table S3 and the corresponding z (A) dependence of p_T-broadening in Table S4 (S5).

SP.4 Tabulated Multiplicity Ratio and p_T-broadening Results This section contains the reported results in the last two figures of this manuscript, Figs. 3 and 4, detailed in Table S6 for all nuclei z-binned multiplicity ratios, and Table S7 (Table S8) for all nuclei z-binned (A-dependent) transverse momentum broadening. In addition, the correlation between z and the Feynman variable x_F is illustrated in Fig. S1 to support the discussion related to the separation between forward and backward fragmentation regions.

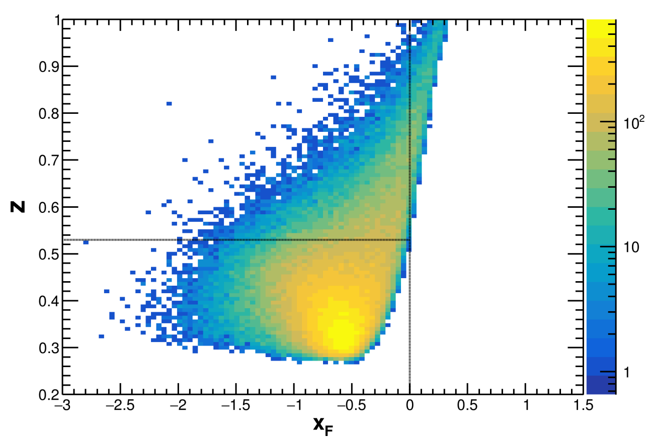

Figure S1. z vs. x_F, where the horizontal dashed line around values of z greater than ≈ 0.55 depicts the discussed separation between forward and backward fragmentation regions suggested by the sign change of x_F (vertical dashed line).

Table S3. Multiplicity ratio systematic effects and their contributions for the z-bins shown in Table S2.

Systematic Effect	z-bin Point-to-point Systematic Uncertainty (%)																	
	Carbon						Iron						Lead					
	$z-1$	$z-2$	$z-3$	$z-4$	$z-5$	$z-6$	$z-1$	$z-2$	$z-3$	$z-4$	$z-5$	$z-6$	$z-1$	$z-2$	$z-3$	$z-4$	$z-5$	$z-6$
Particle identification cuts	0.69	4.24	7.24	1.53	3.16	0.00	0.00	0.95	4.34	0.87	3.17	4.45	8.05	3.21	7.80	0.00	8.59	6.91
Vertex corrections	0.28	0.00	0.04	0.22	0.22	0.54	1.04	1.28	0.56	0.08	0.00	0.13	1.38	1.85	0.13	0.18	0.00	1.01
AC 6D map variables & binning	3.28	0.00	6.69	9.97	9.17	2.33	6.83	4.80	0.00	6.42	5.90	4.93	6.84	0.00	9.05	7.90	6.06	7.23
AC weight cuts	0.00	0.00	10.70	0.70	0.00	0.00	0.00	0.00	9.17	1.86	0.00	0.00	5.17	0.00	8.64	12.16	0.00	0.00
CB uncorrelated-tracks combinations	1.80	0.16	0.37	0.27	0.53	0.00	1.14	0.14	0.20	0.00	0.36	0.23	1.79	2.04	0.96	0.13	0.00	0.28
Breit-Weigner shapes	7.55	10.80	25.75	5.13	8.69	5.77	20.54	16.37	13.40	1.26	0.46	5.27	5.77	12.02	15.71	4.92	10.85	9.52
Λ mass-range	2.10	1.11	0.00	0.86	1.87	2.89	2.52	1.52	0.43	0.00	1.35	2.39	2.24	1.24	0.00	0.65	1.69	2.72
LD2 endcaps	0.06	0.00	0.06	0.09	0.11	0.13	0.03	0.00	0.06	0.08	0.10	0.12	0.07	0.00	0.05	0.07	0.09	0.13
Radiative correction	0.00	2.08	1.26	3.18	1.53	0.94	1.30	1.14	0.29	0.00	0.95	0.21	0.13	0.00	0.81	1.12	0.58	1.90
Total	8.71	11.84	29.61	11.81	13.25	6.93	21.86	17.19	16.82	6.86	6.92	8.81	13.41	12.67	21.58	15.36	15.21	14.20

Table S4. Transverse momentum broadening systematic effects and their contributions for the z-bins shown in Table S2.

Systematic Effect	z-bin Point-to-point Systematic Uncertainty (%)																	
	Carbon						Iron						Lead					
	$z-1$	$z-2$	$z-3$	$z-4$	$z-5$	$z-6$	$z-1$	$z-2$	$z-3$	$z-4$	$z-5$	$z-6$	$z-1$	$z-2$	$z-3$	$z-4$	$z-5$	$z-6$
Particle identification cuts	7.14	0.00	3.77	1.77	0.47	6.03	1.05	8.19	4.97	0.00	0.82	0.87	5.07	2.84	6.24	0.00	3.52	3.24
Vertex Corrections	6.63	8.99	4.62	1.02	0.00	3.99	2.57	2.54	0.00	0.33	0.33	0.67	3.40	1.87	0.81	0.00	0.74	2.79
AC 6D map variables & binning	4.77	6.95	6.02	0.00	8.91	5.49	6.36	9.72	3.05	14.85	0.00	2.20	9.84	7.83	10.52	3.83	7.73	0.00
AC weight cuts	1.83	0.47	18.23	6.74	0.00	0.09	0.00	0.31	13.77	1.52	0.00	0.12	20.17	0.59	19.88	23.63	0.08	0.00
CB sideband subtraction	31.84	0.0	2.1	8.81	0.88	3.79	4.34	2.36	0.0	1.67	7.58	20.32	77.31	8.16	0.0	2.49	6.33	13.28
Radiative correction	3.87	0.24	0.00	0.03	0.00	0.19	0.18	0.28	0.32	0.54	0.00	0.12	5.06	0.49	0.27	0.01	0.00	0.00
Total	33.88	11.38	20.21	11.28	8.96	9.84	8.19	13.18	14.96	15.04	7.63	20.46	80.89	11.84	23.35	24.07	10.62	13.95

Table S5. A-dependent transverse momentum broadening systematic effects and their contributions.

Systematic effect	Point-to-point Systematic Uncertainty (%)		
	Carbon	Iron	Lead
Particle identification cuts	4.69	1.35	0.00
Vertex Corrections	2.70	0.00	0.38
AC 6D map variables & binning	0.57	0.00	2.21
AC weight cuts	3.40	0.00	7.07
CB sideband subtraction	5.52	0.0	2.87
Radiative correction	0.04	0.17	0.00
Total	8.46	1.36	7.96

Table S6. Measured Λ z-binned multiplicity ratios for all nuclei along with their total statistical and systematic (point-to-point and normalization uncertainties depicted in Fig. 3 added in quadrature) uncertainties.

z-bin	R^A_Λ $\pm$ Statistical $\pm$ Systematical Uncertainties		
	Carbon	Iron	Lead
0.28 - 0.38	3.4256 $\pm$ 0.5319 $\pm$ 0.3004	5.7536 $\pm$ 0.5681 $\pm$ 1.2661	7.2363 $\pm$ 0.9997 $\pm$ 0.9893
0.38 - 0.44	1.3447 $\pm$ 0.1603 $\pm$ 0.1628	1.9382 $\pm$ 0.1769 $\pm$ 0.3629	2.6378 $\pm$ 0.3405 $\pm$ 0.3863
0.44 - 0.51	1.1084 $\pm$ 0.1205 $\pm$ 0.3299	2.0100 $\pm$ 0.1735 $\pm$ 0.3674	2.1293 $\pm$ 0.2316 $\pm$ 0.4987
0.51 - 0.60	1.1498 $\pm$ 0.0883 $\pm$ 0.1400	1.2126 $\pm$ 0.0823 $\pm$ 0.1663	1.1857 $\pm$ 0.1057 $\pm$ 0.2659
0.60 - 0.75	1.1174 $\pm$ 0.0756 $\pm$ 0.1519	0.9660 $\pm$ 0.0617 $\pm$ 0.1588	0.8910 $\pm$ 0.0759 $\pm$ 0.2364
0.75 - 1.00	0.9506 $\pm$ 0.1011 $\pm$ 0.0741	0.6450 $\pm$ 0.0529 $\pm$ 0.1549	0.5622 $\pm$ 0.0621 $\pm$ 0.2096

Table S7. Measured Λ z-binned p_T-broadening results for all nuclei with their total statistical and systematic (point-to-point and normalization uncertainties depicted in Fig. 4 left added in quadrature) uncertainties.

z-bin	Δp_T^2 (GeV^2) $\pm$ Statistical $\pm$ Systematical Uncertainties		
	Carbon	Iron	Lead
0.28 - 0.38	0.0003 $\pm$ 0.0143 $\pm$ 0.0015	0.0112 $\pm$ 0.0127 $\pm$ 0.0015	-0.0072 $\pm$ 0.0151 $\pm$ 0.0060
0.38 - 0.44	0.0259 $\pm$ 0.0160 $\pm$ 0.0033	0.0422 $\pm$ 0.0140 $\pm$ 0.0057	0.0592 $\pm$ 0.0171 $\pm$ 0.0071
0.44 - 0.51	0.0648 $\pm$ 0.0174 $\pm$ 0.0132	0.0894 $\pm$ 0.0147 $\pm$ 0.0134	0.0613 $\pm$ 0.0174 $\pm$ 0.0144
0.51 - 0.60	0.1317 $\pm$ 0.0165 $\pm$ 0.0149	0.2120 $\pm$ 0.0168 $\pm$ 0.0319	0.2007 $\pm$ 0.0211 $\pm$ 0.0483
0.60 - 0.75	0.1879 $\pm$ 0.0225 $\pm$ 0.0169	0.2591 $\pm$ 0.0218 $\pm$ 0.0198	0.3140 $\pm$ 0.0295 $\pm$ 0.0334
0.75 - 1.00	0.1145 $\pm$ 0.0157 $\pm$ 0.0114	0.1381 $\pm$ 0.0149 $\pm$ 0.0283	0.1788 $\pm$ 0.0209 $\pm$ 0.0250

Table S8. Measured Λ A-dependent p_T-broadening results for all nuclei along with their total statistical and systematic (point-to-point and normalization uncertainties depicted in Fig. 4 right added in quadrature) uncertainties.

A	Δp_T^2 (GeV^2) $\pm$ Statistical $\pm$ Systematical Uncertainties
Carbon	0.0952 $\pm$ 0.0272 $\pm$ 0.0082
Iron	0.1404 $\pm$ 0.0376 $\pm$ 0.0024
Lead	0.1823 $\pm$ 0.0451 $\pm$ 0.0146